Synchrotron x-ray scattering from metal surfaces nanostructured by IBS

2009 J. Phys.: Condens. Matter 21 224006

(http://iopscience.iop.org/0953-8984/21/22/224006)

IOP Publishing Journal of Physics: Condensed Matter

J. Phys.: Condens. Matter **21** (2009) 224006 (9pp) doi:10.1088/0953-8984/21/22/224006

Synchrotron x-ray scattering from metal surfaces nanostructured by IBS

C Boragno[1] **and R Felici**[2]

[1] Dipartimento di Fisica, Università di Genova, Via Dodecaneso 33, Genova, Italy
[2] European Synchrotron Radiation Facility, BP 220, F-38043 Grenoble, France

Received 26 November 2008
Published 12 May 2009
Online at stacks.iop.org/JPhysCM/21/224006

Abstract

Ion beam sputtering (IBS) can induce the formation of ordered nanostructures, whose properties depend on ion flux, sputtering angle, sample temperature, sample structure, surface symmetry, etc. For the comprehension of the time evolution of the formed nanostructure morphology it is necessary to perform *in situ* real time studies. In this review we shall describe results obtained using x-ray based techniques at synchrotron facilities to study *in situ* the time and temperature evolution of metal surfaces nanopatterned by ion sputtering. Different techniques, such as x-ray reflectivity, grazing incidence small angle x-ray scattering and x-ray surface diffraction have been used, each of them providing complementary information for the determination of the surface structure and morphology. In this review, we present some experiments done in recent years to show how these methods contributed to our understanding of the IBS process on metal surfaces.

1. Introduction

Ion beam sputtering IBS on metal surfaces leads to the formation of nanopatterns whose morphology has been generally studied by using two different kinds of instruments, which can be classified as 'local probes LP' and 'statistical probes SP' methods. The first class comprises methods able to image the surface in real space, such as scanning tunnelling microscopy STM, atomic force microscopy AFM and scanning electron microscopy SEM. All these methods provide a detailed observation of the fine structure of the patterns, including the atomic planes, the shape of the surface defects, and the damage induced by single impact events [1–4]. Generally, these methods have been used in a 'snap-shot' way: the sample is ion bombarded at predetermined conditions, for example fixing the temperature and/or the ion dose, and then it is moved to the imaging position. With LP methods it is relatively easy to follow, in real time, the evolution of the pattern in an annealing experiment, while it is impossible to follow the growth of the pattern during the ion sputtering procedure. This limitation is intrinsic to the LP methods, which require the proximity of a probe to the surface hindering the use of the ion beam at the same time in the same sample region. Among the few exceptions, we must cite the experiment of Habenicht *et al* [5] who were able to ion bombard a graphite surface while the sample was imaged by SEM. In this way, the growth of ripples, their motion on the surface and the variation of the ripple periodicity were recorded in real time but, due to the used method, all information about the surface roughness or the ripple depth were lost.

Another limitation of the LP techniques is that the information is local, since the imaged region is generally of the order of 1 μm^2 or even less. In order to obtain statistical information, it is necessary to collect many images in different regions of the sample, thus increasing the measurement time. This can be a source of problems because metal surfaces can naturally modify their morphology with time at room temperature, so particular care must be taken to 'block' the system, for instance by cooling the temperature until the surface atom diffusion is stopped, to avoid faulty interpretation due to the relaxation of the nanostructures.

Methods holding in the SP class are able to circumvent these limits. Light scattering spectroscopy (LiSSp) [6] is a powerful method to follow, in real time, the pattern growth (for more details, see [34]). A supersonic He beam has been used with a similar aim [7], while spot profile analyser low energy electron diffraction SPA-LEED allows the temperature evolution of the system to be followed in real time [8]. All these methods probe a large region of the sample (several μm square), thus allowing the easy extraction of statistical information on the surface morphology; of course, it is impossible to get details at the atomic level. In addition, these methods explore the morphology in the reciprocal space, and a further modelling effort is often required to get information on the morphology in real space.

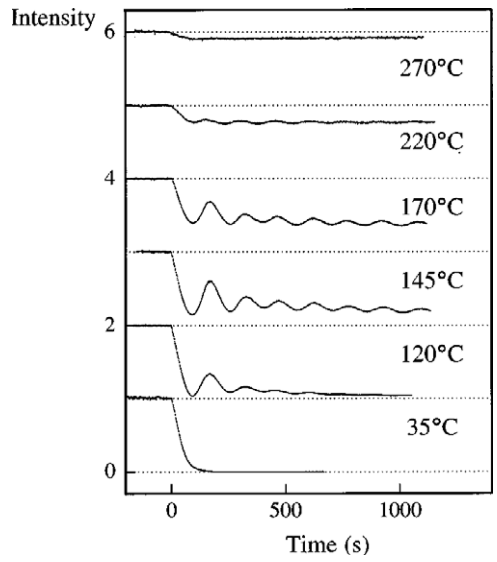

Figure 1. Time and temperature evolution of the x-ray specular beam intensity at a point close to the anti-Bragg position (0 0 1.5) in the reciprocal space during 500 eV Ar^+ irradiation. The curves at different temperatures are offset vertically for clarity. Reprinted with permission from [10]. Copyright 1999 by the American Physical Society.

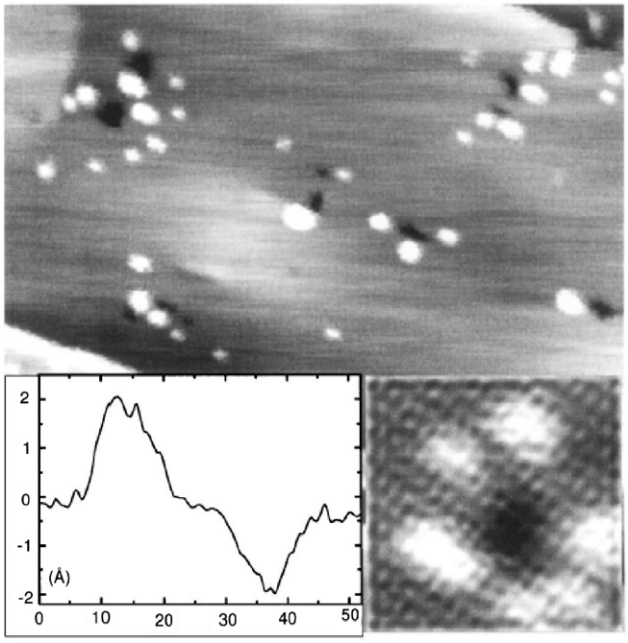

Figure 2. Single ion impact events as seen by STM at low temperature. Experimental conditions: Ag(0 0 1) surface, Ne ion energy 1 keV, surface temperature 115 K. In the upper panel, several single impacts events are resolved (scan area 40 × 23 nm^2); bottom left: a linear scan through an adatom and a vacancy cluster, demonstrating that both have a monoatomic height of about 0.2 nm; bottom right: high resolution image of a single impact event (the atomic lattice has been superimposed by software). Reprinted with permission from [13]. Copyright 2001 by the American Physical Society.

X-ray methods, based on synchrotron radiation facilities, hold in the SP class: they can be applied under different experimental conditions, allowing the surface evolution during the IBS procedure or during an annealing experiment to be followed in real time. Furthermore, due to the specific nature of the probe, they can also be used to investigate what happens in the subsurface region, or to follow the evolution of crystal ordering during the IBS procedure in real time.

In this contribution we focus our attention on the x-ray studies done in recent years on metal samples, with the goal of showing the information which can be extracted from x-ray experiments; similar experiments on semiconductors are the topic of [35].

2. Temperature and time evolution

To our knowledge, the first experiment with x-ray synchrotron radiation on ion sputtered metal samples was done in 1997 by Ramana Murty *et al* [9, 10]. They studied the ion erosion of a Au(111) single crystal whose surface was bombarded with Ar^+ ions with an energy of 500 eV.

Since the main effect of the surface roughness is to decrease the reflected intensity (with a contribution similar to a Debye–Waller term [11]), the authors followed the specular intensity (at a fixed exchanged vertical momentum $q_\perp$) as a function of the sputtering time and surface temperature. As shown in figure 1, different regimes can be identified: at 270 °C, the specular intensity decreases just a little when ion sputtering begins, showing that the roughness increases slightly but rapidly reaches an equilibrium value. Moreover, at this temperature, the peaks belonging to the herringbone reconstruction of a clean Au(111) surface remain unchanged during the IBS procedure. At lower temperatures, in the range from 120 to 220 °C, the reflected intensity decays asymptotically toward a finite value and in this process it shows some intensity oscillation which suggest a layer-by-layer erosion of the surface, analogous to that observed in MBE growth. In this condition, only the first order peaks corresponding to the herringbone reconstruction are still visible. Finally, for temperatures lower than 35 °C the specular intensity decays with time towards zero, indicating a relevant increase of the roughness; in this state, the herringbone reconstruction peaks disappear. Even though reflectivity measurements are not directly sensitive to the formation of nanostructures, all these observations suggest that the surface morphology under ion sputtering must strongly depend on the surface diffusion processes involving adatoms and vacancies created by the ion impacts.

Early STM studies on single ion impact events showed that an ion impinging on a metal surface causes the formation of a vacancy cluster surrounded by a few adatom islands (see figure 2) [12, 13]. Depending on the surface temperature, these defects can move, or can be broken in individual elements, or can be frozen on the surface. Since the time elapsed between two ion impacts in the same region (of the order of 10 × 10 nm^2) is much longer than the time required to reach a stable surface configuration by diffusion, we can assume that each ion always sees the surface in a (quasi-) equilibrium configuration, determined by the diffusion processes which are active at the temperature of the experiment.

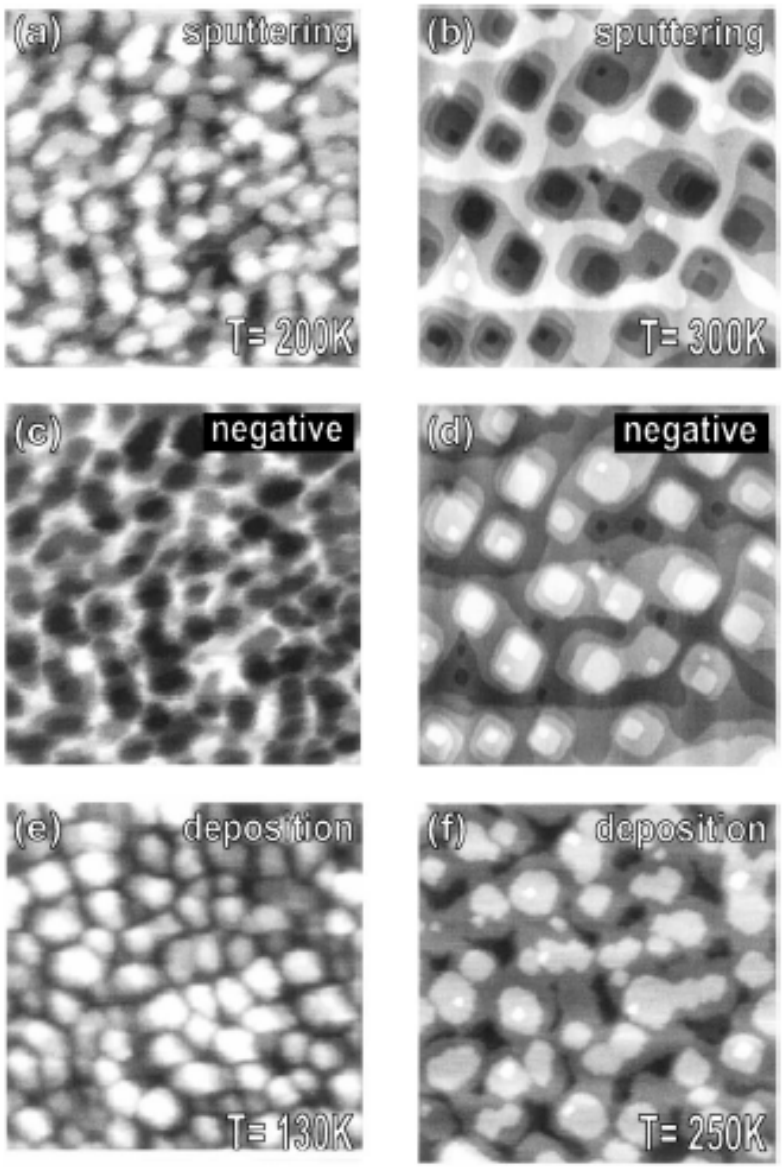

Figure 3. Comparison between surface morphologies obtained by ion sputtering and atomic deposition. The images in the second row are the same as the first row, but with the colour map inverted. Reprinted with permission from [13]. Copyright 2001 by the American Physical Society.

In other words, the IBS process in metals is equivalent to a deposition process, with the difference being that vacancies and adatoms are 'deposited' at the same time in the same region. The final surface morphology will be determined by the competition between the different surface diffusion processes of both adatoms and vacancies.

Clear evidence of this behaviour is reported in figure 3 where the surface morphology after deposition of Ag on Ag(001) is compared to that obtained in an IBS experiment (Ne^+ ions at $E = 1$ keV on the same Ag sample) [13].

At low temperature (column (a)), the morphology in both cases is equivalent (1st and 3rd row): the surface is dominated by (square) mounds which appear to be similar in shape, size and density. On the contrary, the same experiment done at high temperature (column (b)) shows a complementary morphology: the vacancy islands created by IBS (1st row) have a quite similar shape to the adatom islands created by deposition (3rd row). For better visualization, in the 2nd row the colour scale of the 1st image has been inverted, thus substituting mounds with valleys. The conclusion of this experiment is that at low T, ion sputtering is equivalent to an adatom deposition process, while at high T ion sputtering is equivalent to a vacancy deposition process. Since the number and the nature of defects created by an ion impact is practically temperature independent, because of the much higher ion energy as compared to the sample temperature, only different diffusion processes can be responsible of the different morphologies observed.

X-ray results reported in figure 1 can be interpreted by the following model: at high temperature, the damage induced by IBS is rapidly removed by diffusion processes and the surface remains flat and with an high reflectivity. The high degree of local order is seen also from the survival of the herringbone reconstruction. On the contrary, at low temperature many diffusion processes are frozen and the roughness increases monotonically with time. At intermediate

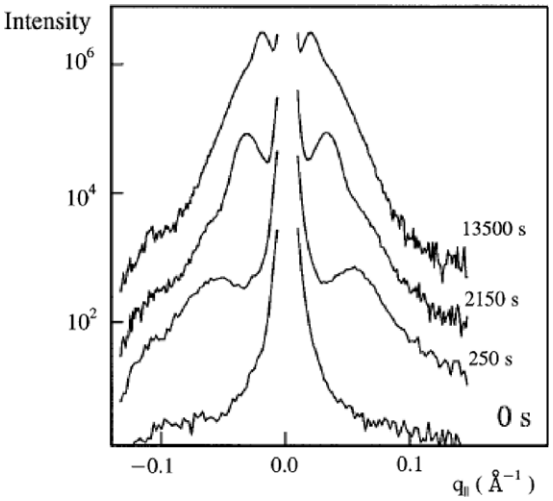

Figure 4. GISAXS spectra recorded after different sputtering times. Reprinted with permission from [10]. Copyright 1999 by the American Physical Society.

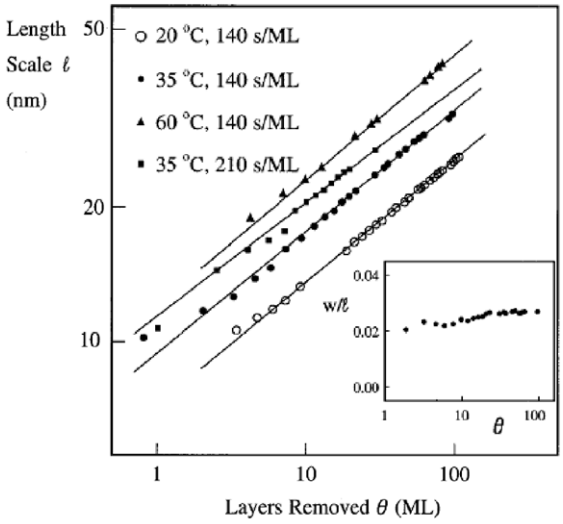

Figure 5. Lateral separation l between surface features as a function of the layers removed (= ion flux × sputtering time) for different temperatures and ion fluxes. In the inset, the ratio between the surface roughness w and l. Reprinted with permission from [10]. Copyright 1999 by the American Physical Society.

temperatures, the oscillatory behaviour revealed by x-ray can be correctly interpreted as the fingerprint of a layer-by-layer erosion regime. We would like to stress that this particular regime could hardly be investigated by LP methods and it demonstrates the power of x-ray methods for a direct evaluation of the time evolution of the surface roughness.

Thus x-ray reflectivity is able to reveal the different IBS regimes, but in order to get more detailed information on the surface morphology it is necessary to use a different approach. Grazing incidence small angle x-ray scattering (GISAXS) can help to determine the surface spatial correlation of the roughness. GISAXS spectra are caused by the x-ray intensity diffused around the specular plane from a rough surface [14]. From a mathematical point of view, the roughness is considered as a small perturbation with respect to the smooth surface. Using Sinha's methodology, the x-ray intensity scattered from a rough surface can be separated into two terms: the first one describing the specular reflection and the second one providing the diffuse scattering. The full treatment of the problem can be found elsewhere [15]. An approximate formula describing the GISAXS intensity scattered from randomly oriented structures onto a flat surface can be written as:

$$I(q) \approx S(q)\langle|F(q)|\rangle^2$$

where $F(q)$ is the form factor of the nanostructures present on the surface (averaged along their possible size distribution and orientation) while $S(q)$ is the correlation function describing their average spatial distribution on the substrate. Measuring the GISAXS intensity it is then possible to determine both the average shape of the nanostructures together with their distribution on the surface ([16, 17]. In the case of nanostructures obtained by IBS, the $\langle|F(q)|\rangle$ function is expected to be a smooth curve having its maximum at $q\| = 0$ and decaying monotonically at larger $q\|$. On the contrary $S(q)$ has its minimum at $q\| = 0$ and goes to 1 at large $q\|$ but in presence of a spatial correlation it is characterized by a maximum at $q\| = q\|_{\max} = 2\pi/l$, where l is the average distance between nanostructures. Therefore a maximum in the GISAXS intensity is closely related (to a first approximation, neglecting the small dependence of $F(q)$) to the average distance between nanostructures.

In figure 4 we show the GISAXS intensity, as measured by Ramana Murty *et al* [9], for a fixed $q_\perp$ of 0.16 Å^{-1} as a function of $q\|$. (i.e. the component of the exchanged momentum parallel to the surface.) On both sides of the specular peak, two clearly resolved (symmetric) shoulders are present, whose intensity grows in time, while their position changes going towards smaller $q\|$.

By following the time evolution of the GISAXS spectra, (see figure 4), it is then possible to follow the evolution of l with the sputtering in real time. Such a dependence is reported in figure 5 in the case of the Au(111) [9, 10].

A scaling law is evident, with an exponent equal to 0.27 ± 0.02. This value is close to the value of 0.25 predicted in a continuum model for the mound formation in a molecular beam epitaxy (MBE) experiment [18]. The presence of a scaling law indicates a relevant coarsening of the surface: again, surface diffusion is responsible for this effect which is less relevant in non-metallic systems and it is poorly considered in the original version of Bradley–Harper model [19].

Similar results and conclusions can be deduced from the experiments done by Malis *et al* [20] on Co(0001) and Kim *et al* [21] on Pd(001). In the latter experiment, x-ray reflectivity XRR has also been extensively used in conjunction with GISAXS scans to determine the temperature and time evolution of the nanopattern induced on the surface by IBS.

3. Determination of the slope of the nanopatterns

So far we have considered the case of isotropic metal surfaces, which the (100) and the (111) surfaces of fcc metals

are. The authors and co-workers have concentrated their attention on the case of anisotropic surfaces, mainly the (110) surface of fcc crystals. Let us consider firstly the case of Ag(110) [22].

In the Ag(110) surface, close-packed rows of atoms run along $\langle 1\bar{1}0\rangle$, whereas in the $\langle 001\rangle$ direction the interatomic distance is $\sqrt{2}$ times the nearest neighbour distances. The surface unit cell is given by $A1$, $A2$, $A3$ which are parallel to the $\langle 1\bar{1}0\rangle$, $\langle 001\rangle$, and $\langle 110\rangle$ directions respectively, with $A1 = A3 = 0.2891$ nm, and $A2 = 0.4089$ nm. The corresponding reciprocal-lattice directions are designed as **H**, **K**, **L**, respectively. Bulk Bragg reflections based on this lattice are found at **H**, **K**, **L** values with $\mathbf{L} = 0, 2, 4, \ldots$ or $\mathbf{L} = 1, 3, 5, \ldots$, depending on whether **H** and **K** have the same or different parity. As is customary in surface x-ray diffraction, the **L** values denote the exchanged momentum perpendicular to the surface. The diffracted intensity is continuously distributed along **L** in the so-called crystal truncation rods CTR, and it contains all the information concerning the structure of the layers terminating the periodic lattice [23].

In the Ag(110) system, the surface diffusion of defects (adatoms and vacancies) is strongly anisotropic, since the diffusion along the channels is faster than across the channels [24]. Therefore we can expect that this asymmetry must be reflected in the nanopattern.

Measurements were carried out at the ID03 beamline of the European Synchrotron Radiation Facility in Grenoble, France. This beamline is devoted to surface x-ray diffraction measurements and is equipped with a large six-circle diffractometer coupled to an UHV chamber with a base pressure of about 10^{-10} mbar. The sample holder is connected to a liquid-nitrogen flow cryostat to cool the sample down to a minimum temperature of 120 K.

The specular reflectivity (at a fixed $q_\perp$) as a function of time (figure 6) shows trends similar to that observed in [9]: at high temperatures the reflectivity decays slightly and approaches a finite value while at low temperatures it decays toward zero. As observed in [9], two temperature regimes are present: for temperatures higher than about 315 K the reflectivity reaches an equilibrium value while for temperatures lower than 315 K the reflectivity always tends to zero with time. However in this low temperature phase three different regimes are observable depending on the decay rate of the reflectivity signal: in the temperature range 290–310 K the roughness evolution is very slow, in the range 230–290 K the roughness evolution is faster and for temperatures lower than 230 K the roughness evolution is extremely fast. Moreover with respect to [9] we have never observed a well-defined temperature region in which the erosion holds in the layer-by-layer regime.

GISAXS spectra have been used to measure the time evolution of the nanopattern: we again found a scaling law of the average distance between nanostructures as a function of the sputtering time, but with a lower exponent (about 0.13, slowly temperature dependent) as compared to the case of the Au(111) surface. In this experiment, we also measured CTR spectra, acquired at different points in the reciprocal space, to determine the shape of the nanostructures at different temperatures.

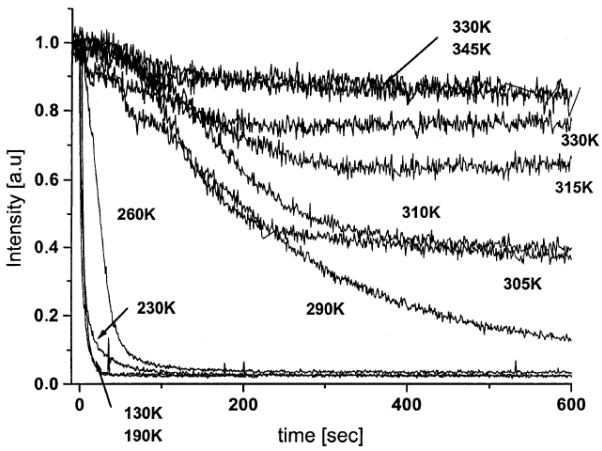

Figure 6. Evolution of the specular intensity as a function of time and temperature during Ag^+ sputtering onto the Ag(110) surface. Reproduced with permission from [26]. Copyright 2002 Elsevier.

As reported in figure 7, at $T = 200$ K a CTR scan along the **H** direction presents two shoulders, which move towards small values as **L** increases; these shoulders are not present in the scan along the **K** direction (i.e. in the perpendicular direction). Since CTR scans are sensitive to the appearance of well aligned facets on the surface [23], we interpreted this result as the presence of elongated structures along the $\langle 001\rangle$ direction, as previously observed by STM [25, 26]. At $T = 270$ K the shoulders are present in both the scans, corresponding to the formation of facets aligned along the two inequivalent surface directions $\langle 1\bar{1}0\rangle$ and $\langle 001\rangle$: the surface morphology is then characterized by the presence of rectangular mounds. Finally, at $T = 320$ K the CTR scans reflect the presence of elongated structures having their edges along the $\langle 1\bar{1}0\rangle$ directions, thus the facets are prevalently oriented along the $\langle 001\rangle$ direction. In this way, we could observe the 'ripple rotation' *in situ*, together with the presence of the mixed phase, already studied by STM [26]. However by using x-rays we can get deeper information on the nanopattern features induced by IBS. In fact, by plotting the peak position as a function of **L** (as measured from several CTR scans), it is possible to determine the local slope of the crystal facets (see figure 8). The local slope was measured at different temperatures after about 1 hour of sputtering at a fixed ion flux (0.056 ML s^{-1}, where 1 ML $= 8.44 \times 10^{14}$ atoms cm^{-2} for Ag(110)).

In figure 9 we compare the local slope determined by x-ray techniques with that determined by analysing several STM images of an Ag(110) surface ion bombarded under similar conditions. The agreement between the two methods is evident, but we would like to stress again that x-ray methods allow a more precise and fast detection of the local slope in ion sputtered metals.

This kind of experiment shows the temperature evolution of the surface morphology induced by IBS on (1 1 0) surfaces. At low temperatures, the surface is organized in ripples having the edges along the slow diffusion $\langle 001\rangle$ direction: we call this nanopattern the low temperature ripple LTR regime. Increasing the temperature, the morphology evolves towards a regular

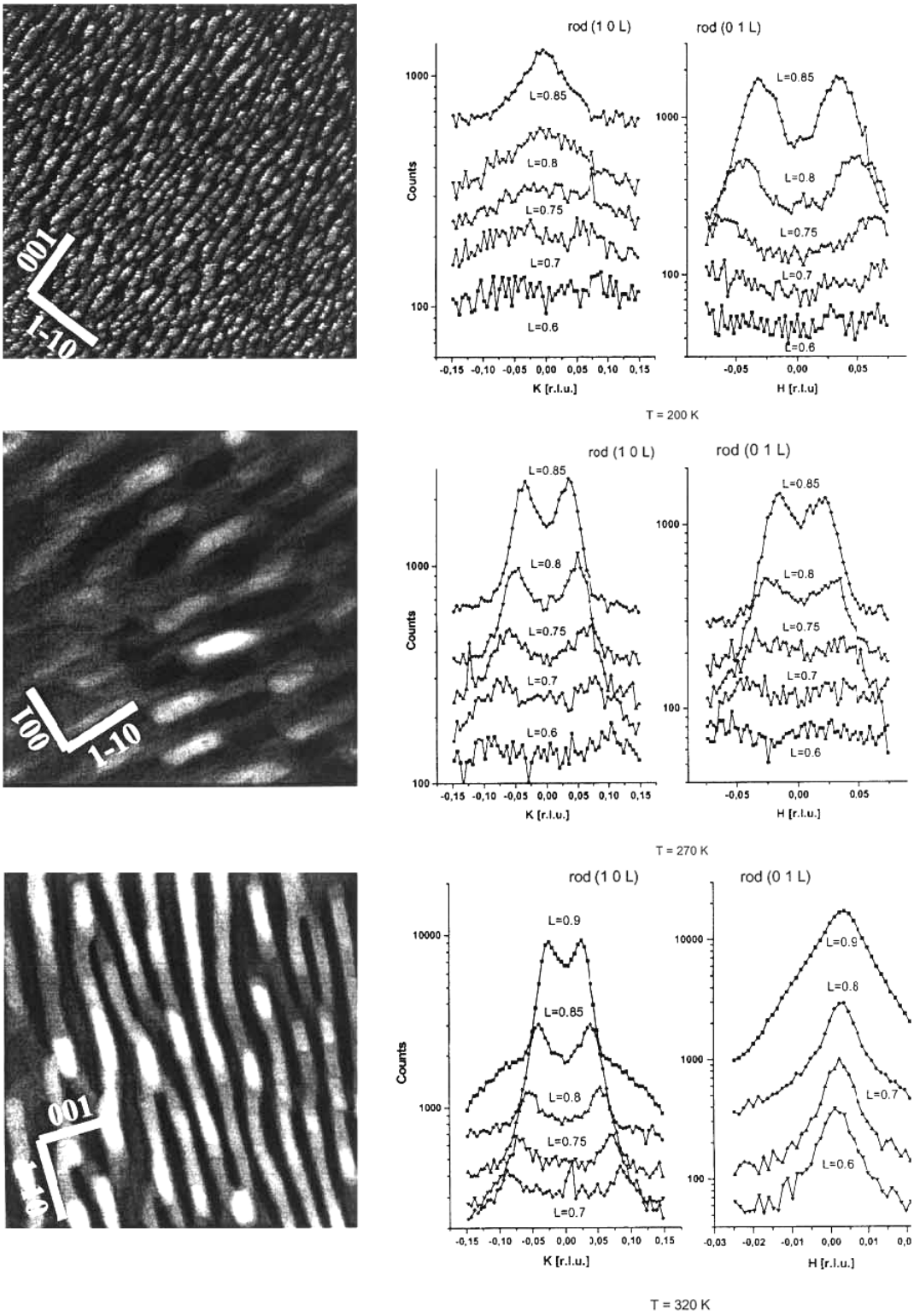

Figure 7. STM images (on the left) and CTR scans (on the right) of an Ag(1 1 0) surface ion bombarded at different temperatures with Ar ions having an energy of 1 keV. Reproduced with permission from [26]. Copyright 2002 Elsevier.

array of rectangular mounds (the rectangular mounds RM regime) and finally it reaches a state characterized by ripples oriented along the fast diffusion $\langle 1\bar{1}0\rangle$ direction (the high temperature ripple HTR regime).

With the same method we have studied several (110) metal surfaces: Ag, Cu, Rh [3, 27, 28] and all of them show a similar behaviour even though the temperature ranges for the LTR and HTR structures are different because of the different activation energy of their diffusion processes. Among all the studied surfaces the only one which never forms ripples is the Pt(110) surface. In this case the IBS leads to the formation of a (1×5) reconstruction, whose structure has been recently

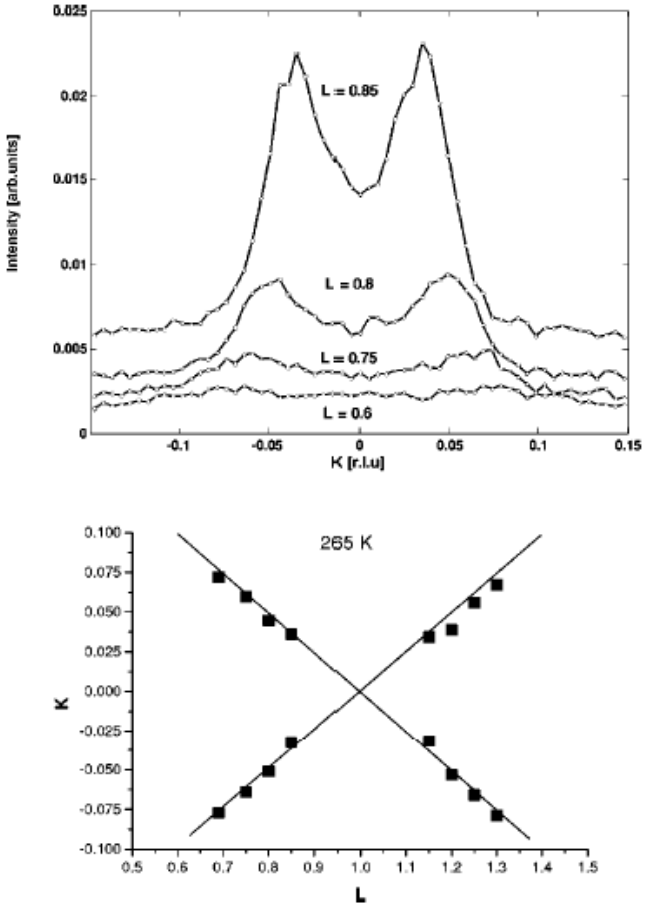

Figure 8. Upper panel: CTR rocking scans acquired at the (1 0 L) position at $T = 265$ K, for various L values, as indicated. The splitting of the CTR is a signature of the faceted surface at a late stage of sputtering. Bottom panel: plot of the peak positions as function of L revealing the average slopes of the facets. Reprinted with permission from [22]. Copyright 2002 by the American Physical Society.

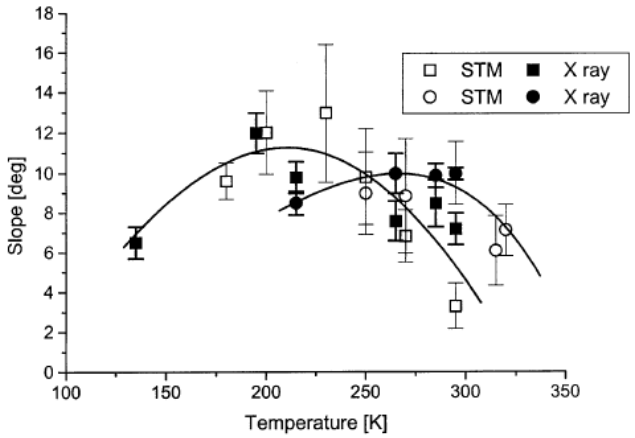

Figure 9. Comparison between the mean facet slope of an ion bombarded Ag(110) surface as determined by CTR scans and STM. Reproduced with permission from [26]. Copyright 2002 Elsevier.

solved by surface x-ray diffraction [29]. We note that the same transition between the different structures has also been observed in MBE experiments [30] and modelled by kinetic Monte Carlo simulations [24].

We applied the same methodology to a more complex problem. In this case, x-ray techniques allow us to get information which hardly could be obtained with other methods [31].

A Cu(110) sample was ion bombarded in a non-symmetric geometry, i.e. with the ion beam impinging on the surface in a direction out of the plane determined by the surface normal and of a principal surface direction, $\langle 1\bar{1}0\rangle$ or $\langle 001\rangle$. With respect to the previous experiment, the angle of incidence was 36° from the normal surface. In this condition, the two facets of the nanopattern created by IBS see two different ion fluxes, one of them being ion bombarded at an angle closer to normal incidence while the other is more at grazing incidence (see inset in figure 10).

This unbalanced situation should be reflected in an asymmetry of the facets of the nanostructures. Following the temperature and time evolution of the system, we obtained the same behaviour observed in Ag(110): a transition between LTR → MR → HTR regimes as a function of the sample temperature. By collecting CTR scans along the **H** or **K** directions while IBS process was active we were able to observe in real time the evolution of the local slope. The main results are collected in figure 10.

At low T, only facets along the $\langle 1\bar{1}0\rangle$ direction are present, as in the previous experiment on Ag(110).

These facets can be clearly resolved only after an ion dose of about 5 ML. However, the two sides of the ripples evolve in different ways: the illuminated side decreases its slope from about 16° to the equilibrium value of 10°, while the other side increase its slope from about 4° to the equilibrium value of 6°. The equilibrium shape is reached after an ion dose of about 20 ML. At 220 and 250 K, where the nanopattern holds in the MR configuration, both the facets are present, but the time evolution of them is quite different: while at 200 K the slope remains more or less constant in time (slope selection), at 250 K we observe a relevant and asymmetric evolution. Again, the equilibrium shape is reached only after an ion dose of about 20 ML. We notice that the effective flux on the I side is about 1.4 times the one on the D side, due to the grazing incidence angle of ions. Therefore, we can expect that the production of defects is larger on the I side by the same amount. That observation could explain the difference in the equilibrium slope on the two sides, but it is more difficult to explain the appearance of the slope selection at 220 K or the similar evolution for the $\langle 100\rangle$ facets on both sides at 250 K. We guess that atomistic simulations (such as kinetic Monte Carlo) could help to understand these observations more deeply.

4. Growth on nanopatterned substrates

Nanopatterns induced by IBS can be used as templates for the subsequent growth of a second material. A good example can be presented by the growth of Co nanoislands on a pre-patterned Cu(110) sample [32]. When Co is deposited onto a flat Cu(110) surface, the film morphology depends on the amount of material deposited: for a coverage of 9 ML the CTR profiles present a broad shoulder around the central peak.

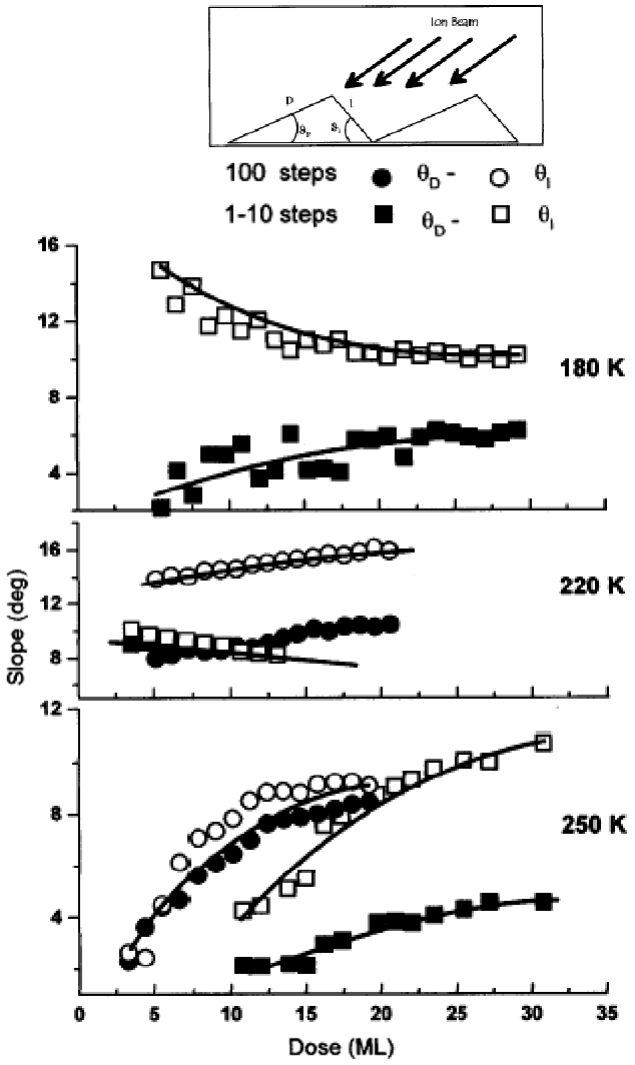

Figure 10. Evolution of the local slope, as determined by CTR scans, as a function of the ion dose for different temperatures. In the upper panel, a sketch showing the experimental geometry. Reprinted with permission from [31]. Copyright 2003 by the American Physical Society.

This feature suggests that the surface morphology is dominated by an uncorrelated roughness at the early stages of growth in agreement with the STM inspections [33]. Above a coverage of 13 ML, this trend changes remarkably and a well-defined pair of satellites appears in the diffraction peak profile. At end, for a film thickness of 24 ML, the satellite splitting increases as **L** moves far from the bulk Bragg reflection point at $\mathbf{L} = 1$, unambiguously confirming the preferential formation of slope selected facets. A quantitative evaluation of the CTR set of data identifies the (1 1 1) orientation of the facet planes, indicating the growth of (1 1 1)-faceted Co nanocrystallites. On the other hand, GISAXS profiles recorded for a 24 ML-thick Co film grown on a flat Cu(110), show that there is no correlation in the lateral distribution of the nanocrystal population.

The film morphology changes significantly if Co is deposited on a pre-patterned Cu(110) surface.

As described before, we formed on the Cu(110) surface an ordered array of rectangular mounds (RM phase) by using

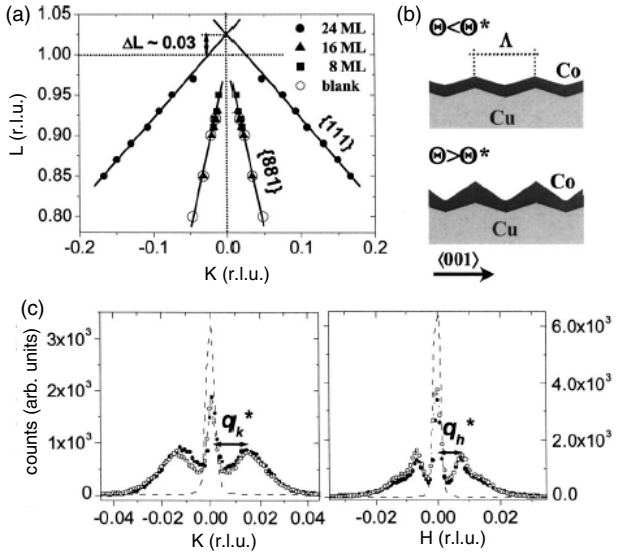

Figure 11. Panel (a) shows the splitting of the satellites around the specular peak as a function of the momentum transfer, indicating the presence of selected facets. Panel (c) shows GISAXS spectra recorded along the two main surface directions before and after Co deposition. Panel (b) sketch showing the surface geometry after the growth of Co nanocrystallites on top of the pre-patterned Cu(110) surface. Reproduced with permission from [32]. Copyright 2005, American Institute of Physics.

IBS. Typical sputtering conditions were: $T = 250$ K, 1 keV Ar^+ ions, incidence angle 30° and ion flux $f = 3\ \mu$A cm^{-2}. Since the average periodicity of the RM pattern undergoes a well-known power law time scaling, it is possible to select the desired pitches between mounds simply by fixing the sputtering time. For instance, after about 75 min of ion irradiation, average mound periodicities of $l_{\langle 1\bar{1}0\rangle} = 38.6 \pm 0.2$ nm and $l_{\langle 001\rangle} = 26.3 \pm 0.4$ nm were achieved, as deduced by GISAXS measurements. Depositing Co on top of this nanopattern, we again found that, for a coverage of 24 ML, Co nanocrystals with (1 1 1) facets were formed, as in the case of a flat surface, but now the nanocrystals were periodically disposed on the surface with the periodicity determined by the IBS procedure.

In figure 11 the main results are summarized. CTR scans reveal that the (1 1 1) facets are well developed only after a deposition of at least 16 ML of Co (panel (a)). For thinner films, the Co islands have a slope of about 10°, comparable to that obtained by IBS. The sketch in panel (b) shows a model of the conformal growth on the pre-patterned surface, while the GISAXS measurements (panel (c)) indicate that the Co nanocrystals are grown on top of the mounds created on Cu by IBS.

Thus, this experiment clearly shows that IBS can be used as a simple method to induce nanopatterns on metals which can drive the growth of an overlayer. It also demonstrates, once again, the usefulness of x-ray methods to study this kind of phenomena.

5. Conclusions

In this paper, we presented a review on the use of x-ray methods to study the shape and morphology of nanopatterns created on metals by IBS. We described some crucial experiments which demonstrate how x-ray reflectivity, GISAXS measurements and CTR scans can provide a lot of information complementary to that obtained by microscopic methods. All these techniques can be used to follow the dynamics of the IBS process in real time as a function of the ion dose and of the temperature.

Acknowledgments

We acknowledge the contribution of many colleagues who participated in the experiments presented in this review, in particular F Buatier de Mongeot, G Costantini, U Valbusa and D Smilgies. The invaluable assistance of the technical staff at ESRF was necessary for the success of this work.

References

[1] Petersen A, Busse C, Polop C, Linke U and Michely T 2003 *Phys. Rev.* B **68** 245410
[2] Hansen H, Redinger A, Messlinger S, Stoian G, Rosandi Y, Urbassek H M, Linke U and Michely T 2006 *Phys. Rev.* B **73** 235414
[3] Rusponi S, Boragno C and Valbusa U 1997 *Phys. Rev. Lett.* **78** 2795
[4] Bose A C and Yoshitake M 2005 *Appl. Surf. Sci.* **241** 174
[5] Habenicht S, Lieb K P, Koch J and Wieck A D 2002 *Phys. Rev.* B **65** 115327
[6] Erlebacher J, Aziz M J, Chason E, Sinclair M B and Floro J A 1999 *Phys. Rev. Lett.* **82** 2330
[7] Bracco G and Cavanna D 2007 *Phys. Rev.* B **76** 033411
[8] Molle A, De Mongeot F B, Molinari A, Boragno C and Valbusa U 2006 *Phys. Rev.* B **73** 155418
[9] Ramana Murty M V, Curcic T, Judy A, Cooper B H, Woll A R, Brock J D, Kycia S and Headrick R L 1998 *Phys. Rev. Lett.* **80** 4713
[10] Ramana Murty M V, Curcic T, Judy A, Cooper B H, Woll A R, Brock J D, Kycia S and Headrick R L 1999 *Phys. Rev.* B **60** 16956
[11] Nevot L and Croce P 1980 *Rev. Phys. Appl.* **15** 761
[12] Michely T and Teichert C 1994 *Phys. Rev.* B **50** 11156
[13] Costantini G, Buatier De Mongeot F, Boragno C and Valbusa U 2001 *Phys. Rev. Lett.* **86** 838
[14] Sinha S K, Sirota E B, Garoff S and Stanley H B 1988 *Phys. Rev.* B **38** 2297
[15] Lazzari R 2002 *J. Appl. Crystallogr.* **35** 406
[16] Revenant C, Leroy F, Lazzari R, Renaud G and Henry C R 2004 *Phys. Rev.* B **69** 035411
[17] Holy V, Roch T, Stangl J, Daniel A, Bauer G, Metzger T H, Zhu Y H, Brunner K and Abstreiter G 2001 *Phys. Rev.* B **63** 205318
[18] Siegert M and Plishcke M 1994 *Phys. Rev. Lett.* **73** 1517
[19] Bradley R M and Harper J M E 1988 *J. Vac. Sci. Technol.* A **6** 2390
[20] Malis O, Brock J D, Headrick R L, Min-Su Yi and Pomeroy J M 2002 *Phys. Rev.* B **66** 035408
[21] Kim T C, Jo M H, Kim Y, Noh D Y, Kahng B and Kim J S 2006 *Phys. Rev.* B **73** 125425
[22] Boragno C, Buatier de Mongeot F, Costantini G, Valbusa U, Felici R, Smilgies D M and Ferrer S 2002 *Phys. Rev.* B **65** 153406
[23] Robinson I K 1986 *Phys. Rev.* B **33** 3830
[24] Hontinfinde F and Ferrando R 2001 *Phys. Rev.* B **63** 121403R
[25] Rusponi S, Costantini G, Boragno C and Valbusa U 1998 *Phys. Rev. Lett.* **81** 2735
[26] Boragno C, Buatier de Mongeot F, Costantini G, Valbusa U, Felici R, Smilgies D M and Ferrer S 2002 *Nucl. Instrum Methods* B **193** 590
[27] Molle A, Buatier de Mongeot F, Molinari A, Xiaerding F, Boragno C and Valbusa U 2004 *Phys. Rev. Lett.* **93** 256103
[28] Rusponi S, Costantini G, Boragno C and Valbusa U 1998 *Phys. Rev. Lett.* **81** 4184
[29] Robinson I K, Saint-Lager M C, Dolle P, Boutet S, De Santis M and Baudoing-Savois R 2005 *Surf. Sci.* **575** 321
[30] Buatier de Mongeot F, Costantini G, Boragno C and Valbusa U 2000 *Phys. Rev. Lett.* **84** 2445
[31] Boragno C, Buatier de Mongeot F, Costantini G, Molle A, de Sanctis D, Valbusa U, Borgatti F, Felici R and Ferrer S 2003 *Phys. Rev.* B **68** 094102
[32] Molle A, Buatier de Mongeot F, Boragno C, Moroni R, Granone F, Sekiba D, Buzio R, Valbusa U, Felici R and Quirós C 2005 *Appl. Phys. Lett.* **86** 141906
[33] Hope S, Gu E, Tselepi M, Buckley M E and Bland J A C 1998 *Phys. Rev.* B **57** 7454
[34] Chason E and Chan W L 2009 *J. Phys.: Condens. Matter* **21** 224016
[35] Carbone D, Biermanns A, Ziberi B, Frost F, Plantevin O, Pietsch U and Metzger T H 2009 *J. Phys.: Condens. Matter* **21** 224007